1mM   10 mM

Concentration-tailored self-assembly composition and function of the coordinating self-assembly of perylenetetracarboxylate

Concentration may direct drastic differences in material composition, structure, and function, which, just like nature, creates diversified materials from limited components.
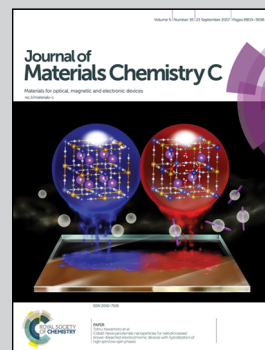
ROYAL SOCIETY
OF CHEMISTRY

rsc.li/materials-c

PAPER

Check for updates

Concentration-tailored self-assembly composition and function of the coordinating self-assembly of perylenetetracarboxylate†

Xuedong Gao, Yijie Wang, Xiaolong Wang, Xuefeng Guo, Jianbin Huang and Yun Yan ID *

Perylene derivatives are excellent n-type dyes that display superior potential in optical and electronic materials. Significant efforts have been endeavored toward structural modification of the perylene skeleton. Herein, we showed that the simple coordinating self-assembly of perylenetetracarboxylate could already generate excellent one-dimensional perylene-based self-assembly, and its structural details could be simply tailored by concentration. Microbelts with high potential energy are formed at concentrations below 1 mM, whereas nanobelts with low potential energy appear at higher concentrations. The coordination stoichiometry was 1 : 1 in the microbelt and 1 : 2 in the nanobelt, which resulted in drastic material properties, such that the microbelt with 1 : 1 coordinated PTC and Ni^{2+} displayed a conductivity 80 times that of the 1 : 2 coordinated nanobelt, whereas the latter exhibited 4 times higher specific surface area, significant fluorescence, and polarized light transmittance. These findings not only unveil a scenario of the coordinating self-assembly of perylenetetracarboxylate, but also show that concentration can act as a powerful tool to tailor the function of self-assembled materials.

Introduction

Perylene derivatives have attracted significant attention in the past two decades owing to their outstanding optical and electronic properties.[1–6] The electron-rich robust π-conjugated plane makes the molecules of this family display excellent thermal stability[7,8] and photostability,[9–11] which are excellent features desired in the fabrication of high quality photovoltaics,[12,13] fluorescence sensors,[9,14] pigments,[1,15] and n-semiconductors.[9,13,16,17] Self-assembly of perylene skeleton is expected to further promote the quality of various perylene-based materials. To this end, diversified modification of the perylene skeleton has been carried out.[9,14,18–21] However, in most cases, one-dimensional structures, such as nanowires,[22–24] nanorods,[19,25,26] nanotubes[27–29] and helices,[30–32] are obtained owing to the dominant growth of self-assembly along the direction of the π–π stacking. Furthermore, a number of efforts are being made with respect to structural modification to create self-assembled one-dimensional perylene

structures in aqueous media to facilitate the formation of environmentally friendly materials.[33,34] Since one-dimensional self-assembled structures of perylene are of significant importance in various applications, much efforts should not be devoted on the structural modification of perylene compounds.

In various strategies of structural modification, researchers usually employ the common material 3,4,9,10-perylenetetra-carboxylic dianhydride as the starting material.[9,14,18–21] This compound is water insoluble and can easily be transformed into sodium and potassium salt simply *via* its dissolution in the aqueous solution of the corresponding base.[35] Most importantly, the simple salt of perylene is able to be assembled into various structures in water *via* ionic or coordination self-assembly.[36–38] For instance, coordination of perylenetetracarboxylate with different metal ions can result in nano plates[39] and nanorods.[19,25] Interestingly, our group found that the coordination self-assembly of perylenetetracarboxylate-Ni displays thermal responsive behavior, in which one-dimensional structures are formed at 4 °C, whereas pinecone structures are formed at 60 °C. Molecular modeling study reveals that intra- and inter-molecular coordination occurs at these two temperatures.[40] This means that kinetic factors are involved in the coordinating self-assembly of perylenetetracarboxylates.

Compared with temperature, concentration is a more economic factor that shows great impact on the reaction kinetics. It is well-known that concentration may affect the speed of chemical equilibrium as well as the size and quality of crystals. In the

Beijing National Laboratory for Molecular Sciences (BNLMS), State Key Laboratory for Structural Chemistry of Unstable and Stable Species, College of Chemistry and Molecular Engineering, Peking University, Beijing 100871, China. E-mail: yunyan@pku.edu.cn

field of molecular self-assembly, a critical concentration is required for starting a self-assembly process. Concentration is even found to affect the supramolecular pathway. For instance, Wesdemiotis and Newkome *et al.* have reported that tetrahedron and bis-rhombus structures are formed at concentrations less than 0.5 mg mL^{-1} and higher than 12 mg mL^{-1}, respectively; this reveals some unexplored effects of concentration.[41] However, the tetrahedron quantitatively reverts to the bis-rhombus upon attempted isolation because these two structures only exist in solution. This prevented the authors from demonstrating the functional difference brought up by the distinct structures. However, this brilliant study suggests that if the concentration-directed self-assembled structures are solids, their functional difference can be expected since the charge carrier mobility is often attributed to a higher degree of order in the solid state, and molecular organization is a key parameter that affects the electronic coupling through π–π molecular interactions.[42–44] Herein, we report the first evidence of the concentration-gated different solid self-assembled perylene-based materials with distinct potential applications. Upon the addition of Ni^{2+} ions to the aqueous solution of perylenetetracarboxylate (PTC), one-dimensional microbelts can be formed at 1 mM. With its composition being PTC : Ni^{2+} = 1 : 1, where the half of the COO$^-$ groups of PTC ion are coordinated to Ni^{2+}, the microbelts have many defects in molecular packing such that they display significant fluorescence and polarized light transmittance. Moreover, the defects also endow the microbelts with larger specific area and higher potential energy. In contrast, at 10 mM, nanobelts with the molar ratio of PTC : Ni^{2+} = 1 : 2 are formed, where all the COO$^-$ groups of PTC are coordinated to Ni^{2+}. This produces a nearly perfect π–π staking of PTC skeleton such that the nanobelts exhibit an extremely high electric conductivity similar to single crystals.

Experiments

1. Fabrication of the PTC/Ni nano and microbelts

The PTC/Ni nano- or micro-structures were obtained by directly vortex mixing the K$_4$PTC solution with metal nitrates solution. In a typical procedure, the stock solutions of 2 mM K$_4$PTC and 4 mM nickel nitrate were mixed in a volume ratio of 1 : 1, and the resulting mixture of 1 mM PTC/2 mM Ni(II) was kept at 4 °C in an incubator for 12 h. Due to the limitation of PTC, the stock solution used in 10 mM PTC/20 mM Ni(II) system was 12 mM K$_4$PTC and 1 M nickel nitrate. The needle crystals that formed during this process were then obtained *via* centrifugation, washed three times with ethanol, and then dispersed in ethanol.

2. Measurements

Scanning electron microscopy (SEM). SEM measurements were performed using a Hitachi S4800 microscope at an acceleration voltage of 10 kV. For SEM measurements, a drop of the suspension (PTC/Ni assemblies dispersed in ethanol) was placed on clean silicon sheets and then dried in the air.

Transmission electron microscopy (TEM) and selected-area electron diffraction (SAED). TEM and SAED images were obtained using a JEM-2100F instrument at an acceleration voltage of 120 kV, which had a symmetrical condenser-objective lens type STWIN (with a spherical aberration C_s = 1.25 mm). A drop of the suspension (PTC/Ni assemblies dispersed in ethanol) was placed on lacey carbon grids and dried in the air before being examined.

Powder X-ray diffraction (XRD). XRD measurements were performed using a Rigaku Dmax-2400 diffractometer with Cu Kα radiation. The samples were vacuum-dried on clean glass slides. Perpendicular direction of (100) face is ⟨100⟩ vector; perpendicular direction of (012) face is ⟨021⟩ vector. PTC molecule stays at the parallel crystal face groups constituting the ⟨100⟩ and ⟨021⟩, where π–π stacking is in the perpendicular direction of the crystal face groups. The vertical vector of the π–π stacking face is ⟨100⟩ × ⟨100⟩ = ⟨0−12⟩, and the crystal face exponent is (0$\bar{2}$1), which corresponds to the π–π stacking. The π–π stacking face for the nanobelts could also be obtained in the same way.

Fluorescence spectra and Ultraviolet-visible (UV-vis) spectro-photometry. Fluorescent measurements were carried out *via* a Horiba-Jobin Yvon Labram HR800 instrument with a 470 nm e–Ne laser with V = 700 V, slit = 5.0 nm, and response time = 2.0 s. A 100× objective (NA = 0.90) was used to focus the laser beam. UV-vis measurements were performed using a Shimadzu UV-1800 spectrophotometer with the slit = 1.0 nm and scan speed = 1.0 nm. Samples were dispersed in ethanol and evenly mixed before being examined. The samples were kept as turbid liquids. The spectral measurements were conducted at room temperature (RT).

Confocal laser scanning microscopy (CLSM) and polarized microscopy. CLSM measurements were carried out using a LeicaTcs-sp A1R-si inverted confocal laser scanning microscope (Nikon, Japan). Polarized microscopy was conducted using an LV1 00Pol88 (Nikon, Japan). One drop of the sample was placed on a clean glass slide and then sealed with a covering glass before being examined.

Fourier transform infrared (FT-IR) spectroscopy. FT-IR spectra were obtained using a Nicolet Magna-IR 750 spectrophotometer (Thermo Scientific Co.). The method of SMART iTR was ART. Scanning speed was 1.0 cm^{-1}. A drop of the suspension (PTC/Ni assemblies dispersed in ethanol) was placed on clean glass slides and dried in the air.

Specific surface area and pore size distribution measurements (BET). BET measurements of the samples were conducted for nanobelts using the ASAP 2010 V6.08 A (Analysis Adsorptive: N$_2$ 77.35 K. N$_2$ adsorption isotherm of microbelts at 77.35 K reveals an uptake of 60.15 cm^3 g^{-1} (4.85 mol/mol, 27.9 wt%) N$_2$ at 800 Torr, which is higher than the N$_2$ uptake of 23.52 cm^3 g^{-1} (3.90 mol/mol, 10.9 wt%)) under the same conditions.

NH$_3$-temperature programmed desorption. NH$_3$-TPD of the samples was tested by chem-BET Plulsar TPD/TPR (quanta-chrome). The micro/nanobelt (100 mg) was purged with nitrogen first, and then, ammonia gas was introduced into the system until the saturated adsorption of ammonia gas was reached. Then, the steam was changed back to nitrogen (30 mL min^{-1}),

This journal is © The Royal Society of Chemistry 2017

J. Mater. Chem. C, 2017, **5**, 8936–8943 | 8937

and after flashing at room temperature for 30 min, the reactor was heated at the rate of 10 K min^{-1}; the signal of NH$_3$ desorption was then detected.

Inductively coupled plasma-atomic emission spectrometer measurement (ICP-AES). The composition of the nano and microbelts was determined using an ICP-AES (PROFILE SPEC, Leeman). Ni^{2+} in the supernate was measured after digestion in concentrated nitric acid for 4 hours and dilution to a constant volume.

The electrical conductivity measurements. The electrical conductivity measurements of micro/nanobelts were carried out using an Agilent 4155C system and a Karl Suss PM5 manual probe station. The gold electrodes separated by 10 μm were fabricated, as previously reported.[45] They were prepared *via* thermal evaporation of gold through a shadow mask on a silicon wafer. Then, a droplet of the suspension was placed on the electrodes and air-dried. This process transferred single microbelt or nanobelt onto the substrate that bridged across two neighboring electrodes. For the measurements under hydrazine atmosphere, a sealed glass jar filled with saturated hydrazine vapor was used, in which the device was placed for 2 h. Then, the device was taken out, and the measurement was performed within 5 min. Control measurements for hydrazine and air showed no conductivity for the electrode system without a bridging crystal. To reduce the negative influence of the fluctuation, 40 electrical devices were measured with a single nanobelt, and the *I–V* curves were treated statistically.

The atomic force microscopy (AFM) measurements. AFM measurements were employed to examine the success of the fabrication of the electronic device for conductivity measurements. AFM for the same sample was conducted in the tapping mode under ambient conditions using a D3100 AFM (VEECO, USA) for electrical conductivity measurements *in situ*. The atomic force microscope (AFM) measures the height of the single belt fabricated from the same device tested in the *I–V* curve, and the SEM measures the weight of single belts *in situ*. As a strong reducing reagent, hydrazine can donate an electron to PTC/M through redox reaction (surface n-type doping), and the doped electrons can rapidly migrate along the belts in the presence of hydrazine.

3. Modeling and theoretical calculations

The coordinating modes and the corresponding energies were calculated at the restricted density functional theory level. The hybrid functional B3LYP and the 6-311+g(d,p) basis set were used. All calculations were performed using the Gaussian09 package. The calculated energy at the most stable state is −1532.9620 a.u. for PTC–4H; −1860.8315 for microbelts PTC–1Ni; and −2197.2279 a.u. for nanobeltsPTC–2Ni. For nanobelts, the contribution of the reduced system energy for each Ni atom is −166.07 a.u. and −163.93 a.u. for microbelts.

$$\Delta\varepsilon' = \frac{-1860.8315 - (-1532.9620)}{2} = -163.93 \text{ a.u.}$$

$$\Delta\varepsilon'' = \frac{-2197.2279 - (-1532.9620)}{4} = -166.07 \text{ a.u.}$$

$$\Delta\varepsilon = \Delta\varepsilon' - \Delta\varepsilon'' = -163.93 - (-166.07) = -2.14 \text{ a.u. Hartree}^{-}.$$

Thus, the restricted density functional calculation suggests that

the potential energy for the PTC–2Ni mode is 2.14 Hartree lower than that of the PTC–Ni.

Results and discussion

The self-assembled system herein is based on the potassium salt of 3,4,9,10-perylenetetracarboxylic potassium (PTC) (Fig. 1a) and Ni(NO$_3$)$_2$. PTC forms a transparent solution in water at concentrations below 10 mM. However, needle-like precipitations immediately occurred upon the addition of aqueous solution of Ni(NO$_3$)$_2$ at the molar ratio of PTC:Ni^{2+} = 1:2. Strikingly, as the concentration of PTC increases from 1 mM to 10 mM, the precipitates changes from yellow to dark red (Fig. 1b); this indicates the formation of different materials (Fig. 1a). SEM images in Fig. 1c–f reveal the formation of one-dimensional belts at all these concentrations, but the size of these belts is
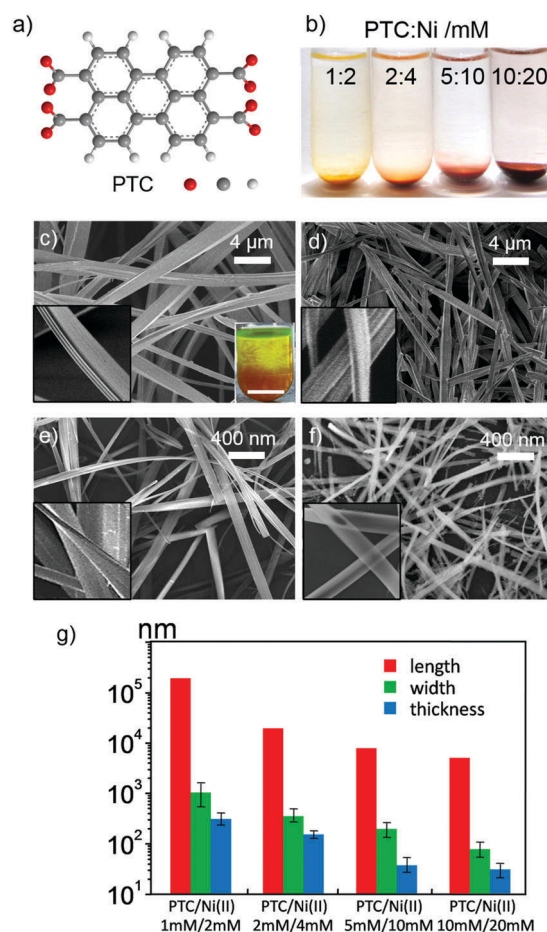

Fig. 1 (a) Schematic of the chemical structure of perylenetetracarboxylate ion (PTC). (b) The images of the PTC:Ni = 1:2 system at different concentrations in ethanol. (c–f) SEM images of the self-assemblies formed in 1 mM PTC/2 mM Ni(ɪɪ) (c), 2 mM PTC/4 mM Ni(ɪɪ) (d), 5 mM PTC/10 mM Ni(ɪɪ) (e), and 10 mM PTC/20 mM Ni(ɪɪ) (f). The inset in (c–f) shows the images of enlarged view of the selected section. All the systems are incubated at 4 °C for 24 h. (g) Histogram of the size distribution of the precipitates obtained at different concentrations. The crystal like precipitates were obtained by centrifugation, washed with ethanol, and dispersed in ethanol for SEM observation.

8938 | *J. Mater. Chem. C*, 2017, **5**, 8936–8943

This journal is © The Royal Society of Chemistry 2017

dramatically different. In the dilute system of 1 mM PTC/2 mM Ni^{2+}, the length, width, and thickness of the belt are about 200 μm, 30 μm, and 200 nm, respectively, whereas these values gradually reduce to 20 μm, 50 nm, and 15 nm as the concentration is increased to 10 mM PTC/20 mM Ni^{2+}. The histogram of the size distribution in Fig. 1g shows the transition from micrometer wide belts (microbelts) to nanometer wide belts (nanobelts) with the increasing starting concentrations. Since an increase in concentration is well-known to lead to smaller precipitates or crystals due to the generation of more crystal seeds, control experiments without the addition of metal ions have been conducted to examine the primitive structures formed in the 1 mM and 10 mM PTC solutions. Fig. S1 (ESI†) reveals that the original self-assembly in the 1 mM PTC system is small plates, whereas large plates are formed in the 10 mM system; this excludes the possibility of formation of more crystal seeds with the increasing concentration. Obviously, the formation of smaller nanobelt in the 10 mM PTC/20 mM Ni^{2+} system has a different mechanism.

FT-IR measurements (Fig. 2a) show that both the micro and nanobelts display similar asymmetric ($1593 \ cm^{-1}$) and symmetric ($1430 \ cm^{-1}$) stretching vibration of C=O. The frequency separation $\Delta\nu = \nu_{as}(COO) - \nu_{s}(COO) = 163 \ cm^{-1}$ indicates bidentate chelating coordination in both structures.[46–48] However, an extraordinary absorption peak in $1640 \ cm^{-1}$ appears in the IR spectra of the microbelts, indicating the presence of un-coordinated carboxylate groups.[48] This means that the molar ratio between Ni and PTC in these two 1D structures is probably different. Indeed, elemental analysis reveals that the molar ratio of PTC : Ni is 1 : 2 in the nanobelt and 1 : 1 in the microbelt (Fig. S2 and Table S1, ESI†).

The difference in the composition indicates that the molecular arrangements in these two 1D structures are different, which is further reflected in their fluorescence. The images in Fig. 2b

reveal that the microbelt displays weak fluorescence, whereas fluorescence for the nanobelt is undetectable to the naked eye. Compared with the strong fluorescence of the PTC solution in 10 mM solution, fluorescence quenching occurred in both the micro and nanobelts. The normalized emission spectra indicate that both the emission for the microbelt and nanobelt have red-shifted; this indicates that the fluorescence quenching originates from the π–π stacking of the PTC skeletons in both the structures.[32,49,50] The emission for the nanobelt is redder than that for the microbelt; this suggests that the PTC molecules have a better π–π stacking state in the nanobelt, which is in line with the stronger fluorescence quenching in the nanobelts.[51,52]

Powder X-ray diffraction (XRD) and selected-area electron diffraction (SEAD) measurements provide deeper insight into the molecular packing in the solid state of PTC/Ni^{2+} micro/ nanobelt. The microbelt displays four intense X-ray diffraction peaks at 2θ = 6.66°, 7.26°, 12.08°, and 26.93° (Fig. 2c) corresponding to lattice spacings of 1.33, 1.22, 0.74, and 0.34 nm, respectively. The d-spacing of 0.34 nm is the characteristic of π–π stacking, which further confirmed the conclusion derived from the fluorescence measurements.[49,53,54] The diffraction indexes derived from these spacings are (hkl) = (101), (110), (012), and (12$\bar{1}$), featuring a simple trigonal crystal structure (space group $R\bar{3}$, number 148).[55–57] In contrast, the XRD pattern for the nanobelt is drastically different. Herein, six diffraction peaks at 2θ = 6.20°, 6.71°, 12.21°, 16.39°, 26.85°, and 27.53° were observed, corresponding to the lattice spacings of 1.44, 1.32, 0.73, 0.55, 0.33, and 0.32 nm, respectively. The resulting lattice index (hkl) is derived to be (100), (020), (012), (003), (143), and (0$\bar{2}$1), featuring an oblique crystal structure (space group $P1$, number 1). Notice that the diffraction peak from the π–π stacking becomes extremely strong and sharp in the nanobelt;
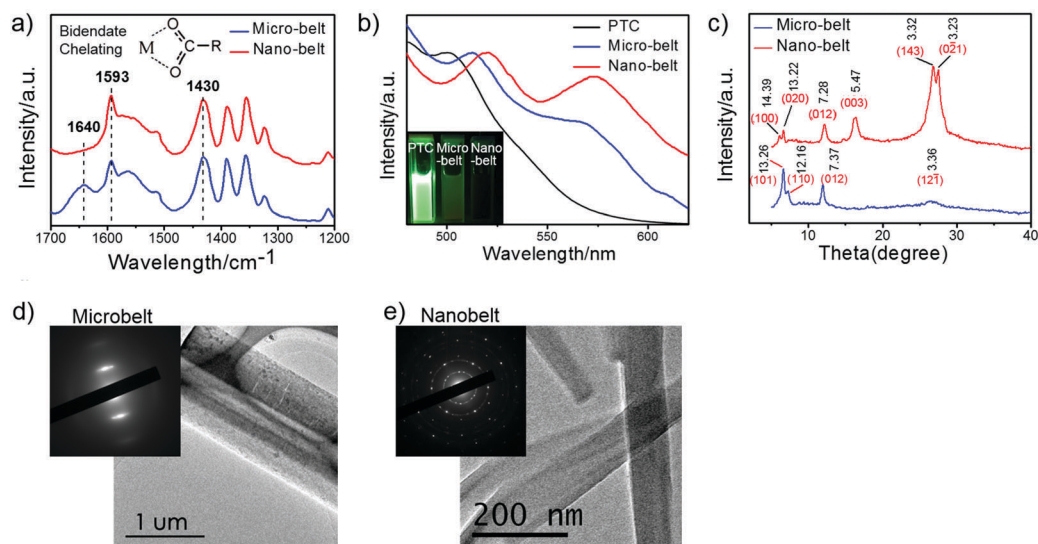

Fig. 2 (a) The FT-IR spectra for the microbelt (blue line) and nanobelt (red line). Inset: Schematic of bidentate coordination of COO group with Ni^{2+}. (b) Normalized fluorescence emission spectra of 1 mM PTC, PTC–Ni microbelt, and PTC–2Ni nanobelts in ethanol. The excitation is at 470 nm, inset is the image obtained under 356 nm irradiation. The microbelt and nanobelt are insoluble in ethanol, and the measurements were made for their dispersions. (c) XRD patterns of the two structures in the powder state. The unit of inserted distances is Å. SEAD pattern of a single microbelt (d) and nanobelt (e). The TEM image shows the diffraction position for the SEAD measurements.

this suggests that the PTC planes have been packed in a crystalline nature along the long axis of the nanobelt. Moreover, the π–π stacking distance has been reduced to 0.32 nm;[49,53,54] this also indicates that extremely strong π–π interaction has occurred in the nanobelts. In line with the XRD patterns, sharp diffraction spots can be clearly visualized in the selected area electron diffraction (SAED) for the nanobelt (Fig. 2e), whereas only a light minor arc is observed for the microbelt (Fig. 2d and Fig. S3, ESI†).

Restricted density functional calculation and molecular modeling is adopted to understand the molecular packing of the PTC skeleton at the molecular level (see details for the modeling method in ESI†). The torsion angle of the PTC plane is about $9.2°$ in the PTC:Ni = 1:1(microbelt) system (Fig. 3a, b and e), whereas it is about $5.5°$ in the PTC:Ni^{2+} = 1:2 (nanobelt) system (Fig. 3c–f). This explains why a better π–π stacking occurs in the nanobelts. Furthermore, the calculation suggests that the potential energy for the PTC:Ni^{2+} = 1:2 mode is 2.14 Hartree lower than that of the PTC–Ni (ESI†). Obviously, the microbelt composed of PTC: Ni^{2+}= 1:1 is a kinetic trapped structure. Fig. 4a shows that only nanobelts were observed when the dried microbelt was incubated for 5 days in the supernatant of nanobelts; this suggests that the microbelt will finally transform into the thermally stable nanobelt. However, this transition can only occur in the presence of a solvent; both the microbelt and nanobelt are very stable with time in the dry state at room temperature.

We expect that the kinetic trap at low concentrations is related to the steric barriers encountered by the second Ni^{2+} that tends to bind to the remaining COO^- group in the PTC skeleton. Since the concentration is low, the collision between Ni^{2+} ions and the PTC skeleton is less such that only few ions can surpass this barrier. However, with the increasing concentration, the increased probability of collision allows more ions to surpass the barrier; this can further lead to the formation of thermally stable nanobelt with the coordination stoichiometry of 1:2. As an

evidence of this scenario, the stoichiometry was found to change gradually with the increasing concentration. Exact 1:1 and 1:2 compositions were found at concentrations below 1 mM and 10 mM, respectively, whereas in-between were the structures with intermediate stoichiometry (Fig. 4b).

The different coordination stoichiometry and the molecular arrangement in the microbelt and nanobelt indicate that the two one-dimensional materials may have completely different properties. First, the less ordered π–π stacking allows the microbelt to display larger specific surface area and considerable fluorescence. The BET measurements, as shown in Fig. 4c, suggest that the microbelts have a higher surface area of 142 $m^2 g^{-1}$ and a smaller pore size of 4.9 nm, whereas the nanobelts have a smaller surface area of 35 $m^2 g^{-1}$ and a bigger pore size of 12 nm. This means that the microbelt has higher storage capacity of gases as compared to nanobelts. Indeed, the adsorption capacities of NH_3 are 4.732 mM NH_3 per g for microbelt and 1.839 mM NH_3 per g for nanobelt, confirming the strong adsorption ability of the microbelts.

Furthermore, the defects in the π–π stacking of the PTC backbone allow preservation of fluorescence of the PTC molecule in the microbelts. CLSM image clearly shows that the microbelts are sufficiently emissive, whereas the emission from the nanobelts can be hardly observed. The microbelts emit green and yellow light under excitation at 488 and 543 nm, respectively (Fig. 4d); this implies their potential to be used as multicolor emission materials. Most interestingly, polarized light transmittance has been observed, confirming that the PTC molecules have oriented properly in the microbelts. Fig. 4e shows the optical observation of a single microbelt under a polarizer (Fig. 4f–i). As the angle of the polarizer changes, the lightness varies accordingly. The multicolor fluorescence emission together with the ability to polarize light endows the microbelt with great potential in the field of advanced optical materials.

However, the perfect stacking of PTC in the nanobelt endows better electrical conductivity. The average derivation
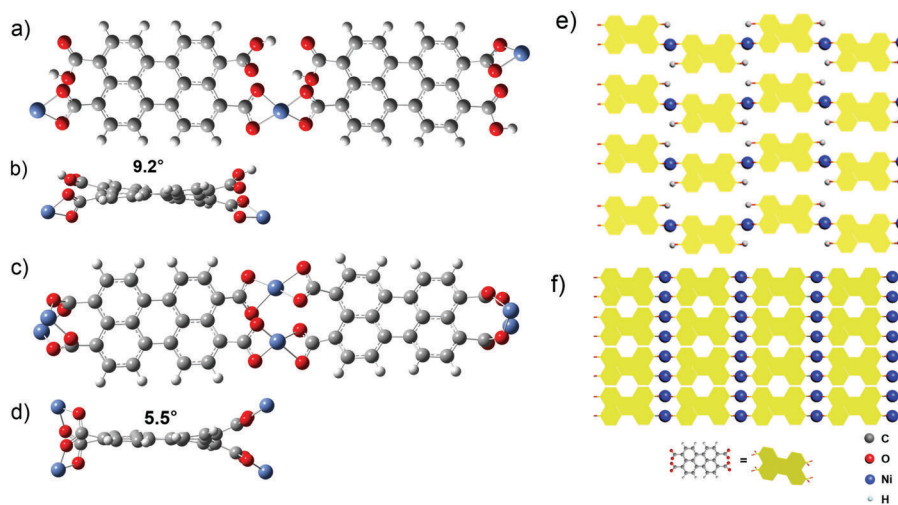

Fig. 3 Molecular modeling of the coordinating states between PTC and the metal ion. (a and b) are the side and front views of the un-saturated coordinating PTC–Ni system; (c and d) are those for the saturated coordinating PTC–2Ni system; (e and f) are the bulk molecular arrangement in the microbelt (PTC–1Ni) and nanobelt (PTC–2Ni), respectively.

8940 | J. Mater. Chem. C, 2017, 5, 8936–8943

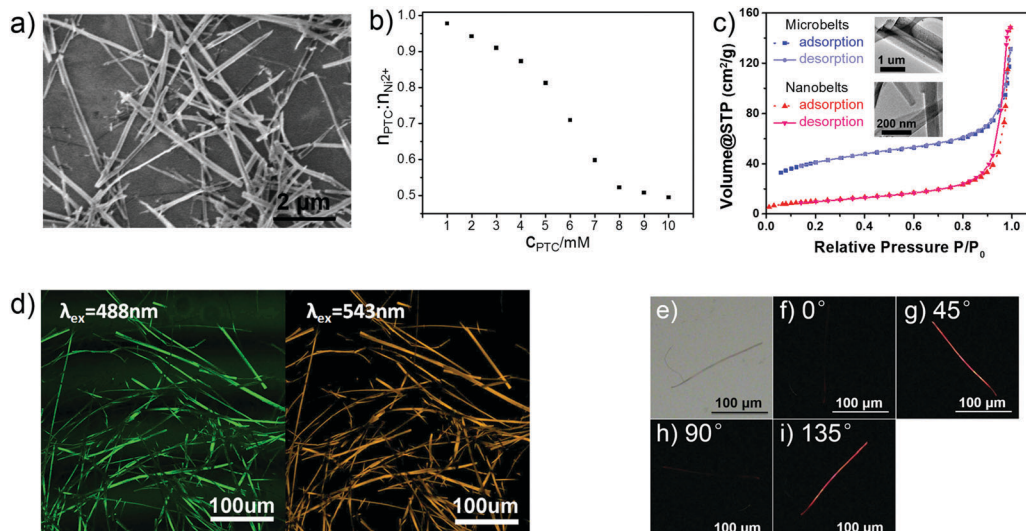This journal is © The Royal Society of Chemistry 2017

Fig. 4 (a) SEM image of the microbelt incubated in the saturated solution of the nanobelt. (b) The fraction of PTC/Ni(II) complex variation in precipitates with the increasing concentration. (c) N_2 adsorption−desorption isotherm of microbelt (blue) and nanobelt (red). (d) Fluorescence image of PTC/Ni(II) microbelts excited at 488 nm and at 543 nm. (e−i) are the polarized microscopy images of one microbelt before (e) and after inserting the polarizer in 0° (f), 45° (g), 90° (h), and 135° (i).
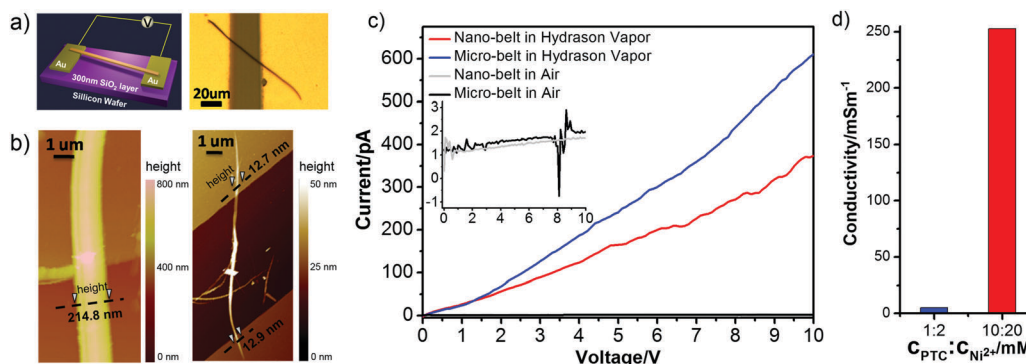

Fig. 5 (a) Schematic and optical microscopy image of electrodes connected by a single belt, where the silicon wafer acts as a global back-gate; (b) AFM images are in situ measurement of microbelt (left) and nanobelts (right) corresponding to the I−V curve in situ. (c) I−V curve of a PTC/Ni^{2+} belt deposited across a pair of Au electrodes at a gate bias of 0 V. (d) Conductivities obtained from the I−V curves for the micro and nanobelt. The nanobelt was made from 10 mm PTC : 20 mM Ni^{2+}, and the microbelt was made from 1 mM PTC and 2 mM Ni^{2+}.

of conductivity for the microbelt is 3.19 mS m^{-1}, which is comparable to that of other belt structures of perylene derivatives such as perylenetetracarboxydiimide and K$_4$PTC.[32,35,58,59] Strikingly, the average conductivity for the nanobelt is as high as 253 mS m^{-1}, which is 80 times that of the microbelts (Fig. 5c). This extremely high electrical conductivity of the nanobelt indicates that the perfect π–π stacking of the PTC groups facilitates efficient charge transportation, which enables fast charge collection at electrodes and reduces the charge recombination within the highly ordered nanowire.[60] In comparison with nanowires and nanobelts reported previously,[46,61] the conductivity of the nanobelt herein is much higher than that of the perylene,[32,35,58,59] porphyrin,[61] or tetrathiafulvalene[45] derivatives, and it is even comparable to those of single crystalline arrays of perylenedianhydride.[62] To the best of our knowledge, the nanobelt formed with PTC : Ni^{2+} = 1 : 2 is one of the best molecular semiconductors generated via self-assembly.[6,63]

Conclusion

In summary, we report the first evidence of concentration-directed drastic material function using the coordinating self-assembly of perylenetetracarboxate (PTC) and nickel ion (Ni^{2+}). At low concentrations, kinetically trapped structure of microbelt with the composition of PTC : Ni^{2+} = 1 : 1 is formed, whereas thermally stable nanobelt with the composition of PTC : Ni^{2+} = 1 : 2 is formed at higher concentrations. The packing of PTC in these two structures is drastically different. Defects in the molecular packing exist in the microbelts, which endow the microbelts with higher specific surface area, significant fluorescence, and ability to polarize light, whereas the PTC molecules adopt nearly perfect π–π stacking in the nanobelt; this leads to extremely high electrical conductivity similar to that generated by single crystals. This study shows the first evidence stating

that low concentration can result in kinetically trapped structures, which not only unveil a hidden world of concentration, but also envision that concentration can be rationally employed in the design of various advanced materials through the approach of kinetic trap.

Competing financial interest

The authors declare no competing financial interest.

Acknowledgements

References

1 F. Wurthner, *Chem. Commun.*, 2004, 1564.
2 T. Kimoto, T. Amako, N. Tajima, R. Kuroda, M. Fujiki and Y. Imai, *Asian J. Org. Chem.*, 2013, **2**, 404.
3 C. E. Mills, A. Obermeyer, X. Dong, J. Walker and B. D. Olsen, *Langmuir*, 2016, **32**, 13367.
4 H. Langhals, *Heterocycles*, 1995, **40**, 477.
5 P. Spenst, R. M. Young, B. T. Phelan, M. Keller, J. Dostal, T. Brixner, M. R. Wasielewski and F. Wuerthner, *J. Am. Chem. Soc.*, 2017, **139**, 2014.
6 Y. Han, W. Ning, L. Cao, X. Xu, T. Li, F. Zhang, L. Pi, F. Xu and M. Tian, *Nano Res.*, 2016, **9**, 1948.
7 Y. Zheng, H. Long, G. C. Schatz and F. D. Lewis, *Chem. Commun.*, 2005, 4795.
8 U. Hahn, S. Engmann, C. Oelsner, C. Ehli, D. M. Guldi and T. Torres, *J. Am. Chem. Soc.*, 2010, **132**, 6392.
9 D. Goerl, X. Zhang and F. Wuerthner, *Angew. Chem., Int. Ed.*, 2012, **51**, 6328.
10 F. Wurthner, C. Thalacker, A. Sautter, W. Schartl, W. Ibach and O. Hollricher, *Chem. – Eur. J.*, 2000, **6**, 3871.
11 M. D. Rahn, T. A. King, A. A. Gorman and I. Hamblett, *Appl. Opt.*, 1997, **36**, 5862.
12 Y. Zhong, M. T. Trinh, R. Chen, W. Wang, P. P. Khlyabich, B. Kumar, Q. Xu, C.-Y. Nam, M. Y. Sfeir, C. Black, M. L. Steigerwald, Y.-L. Loo, S. Xiao, F. Ng, X. Y. Zhu and C. Nuckolls, *J. Am. Chem. Soc.*, 2014, **136**, 15215.
13 C. Li and H. Wonneberger, *Adv. Mater.*, 2012, **24**, 613.
14 X. Zhang, S. Rehm, M. M. Safont-Sempere and F. Wuerthner, *Nat. Chem.*, 2009, **1**, 623.
15 C. Huang, S. Barlow and S. R. Marder, *J. Org. Chem.*, 2011, **76**, 2386.
16 X. Zhang, Z. Lu, L. Ye, C. Zhan, J. Hou, S. Zhang, B. Jiang, Y. Zhao, J. Huang, S. Zhang, Y. Liu, Q. Shi, Y. Liu and J. Yao, *Adv. Mater.*, 2013, **25**, 5791.
17 F. Wuerthner and M. Stolte, *Chem. Commun.*, 2011, **47**, 5109.
18 E. Krieg, E. Shirman, H. Weissman, E. Shimoni, S. G. Wolf, I. Pinkas and B. Rybtchinski, *J. Am. Chem. Soc.*, 2009, **131**, 14365.
19 D. Goerl, X. Zhang, V. Stepanenko and F. Wuerthner, *Nat. Commun.*, 2015, **6**, 7009.
20 J. T. Kirner, J. J. Stracke, B. A. Gregg and R. G. Finke, *ACS Appl. Mater. Interfaces*, 2014, **6**, 13367.
21 S. Bai, S. Debnath, N. Javid, P. W. J. M. Frederix, S. Fleming, C. Pappas and R. V. Ulijn, *Langmuir*, 2014, **30**, 7576.
22 R. Marty, R. Nigon, D. Leite and H. Frauenrath, *J. Am. Chem. Soc.*, 2014, **136**, 3919.
23 R. Marty, R. Szilluweit, A. Sanchez-Ferrer, S. Bolisetty, J. Adamcik, R. Mezzenga, E.-C. Spitzner, M. Feifer, S. N. Steinmann, C. Corminboeuf and H. Frauenrath, *ACS Nano*, 2013, **7**, 8498.
24 A. Datar, K. Balakrishnan and L. Zang, *Chem. Commun.*, 2013, **49**, 6894.
25 Y. Tidhar, H. Weissman, S. G. Wolf, A. Gulino and B. Rybtchinski, *Chem. – Eur. J.*, 2011, **17**, 6068.
26 L. Kang, Z. Wang, Z. Cao, Y. Ma, H. Fu and J. Yao, *J. Am. Chem. Soc.*, 2007, **129**, 7305.
27 C. Backes, F. Hauke and A. Hirsch, *Adv. Mater.*, 2011, **23**, 2588.
28 Y. Liu, K.-R. Wang, D.-S. Guo and B.-P. Jiang, *Adv. Funct. Mater.*, 2009, **19**, 2230.
29 Y. Che, A. Datar, K. Balakrishnan and L. Zang, *J. Am. Chem. Soc.*, 2007, **129**, 7234.
30 V. Stepanenko, X.-Q. Li, J. Gershberg and F. Wuerthner, *Chem. – Eur. J.*, 2013, **19**, 4176.
31 L. Xue, N. Ranjan and D. P. Arya, *Biochemistry*, 2011, **50**, 2838.
32 Z. X. Wei, T. Laitinen, B. Smarsly, O. Ikkala and C. F. J. Faul, *Angew. Chem., Int. Ed.*, 2005, **44**, 751.
33 T. Tang, K. Peneva, K. Muellen and S. E. Webber, *J. Phys. Chem. A*, 2007, **111**, 10609.
34 G. Schnurpfeil, J. Stark and D. Wohrle, *Dyes Pigm.*, 1995, **27**, 339.
35 G. H. Fu, M. L. Wang, Y. L. Wang, N. Xia, X. J. Zhang, M. Yang, P. Zheng, W. Wang and C. Burger, *New J. Chem.*, 2009, **33**, 784.
36 Y. Liang, H. Wang, D. Wang, H. Liu and S. Feng, *Dyes Pigm.*, 2012, **95**, 260.
37 X.-h. Cheng, Y. Peng, C. Gao, Y. Yan and J.-b. Huang, *Colloids Surf., A*, 2013, **422**, 10.
38 X. Ren, W. Yu, Z. Zhang, N. Xia, G. Fu, X. Lu and W. Wang, *Colloids Surf., A*, 2011, **375**, 156.
39 M. Huang, U. Schilde, M. Kumke, M. Antonietti and H. Colfen, *J. Am. Chem. Soc.*, 2010, **132**, 3700.
40 Y. Wang, X. Gao, Y. Xiao, Q. Zhao, J. Yang, Y. Yan and J. Huang, *Soft Matter*, 2015, **11**, 2806.
41 X. Lu, X. Li, K. Guo, T.-Z. Xie, C. N. Moorefield, C. Wesdemiotis and G. R. Newkome, *J. Am. Chem. Soc.*, 2014, **136**, 18149.
42 J. Hieulle and F. Silly, *J. Mater. Chem. C*, 2013, **1**, 4536.
43 S.-L. Lee, H.-J. Wu, Y.-J. Hsu, H.-H. Chen, H.-F. Hsu and C.-h. Chen, *Chem. Commun.*, 2014, **50**, 14093.
44 K. M. Lefler, C. H. Kim, Y.-L. Wu and M. R. Wasielewski, *J. Phys. Chem. Lett.*, 2014, **5**, 1608.
45 Y. Qiao, Y. Lin, S. Liu, S. Zhang, H. Chen, Y. Wang, Y. Yan, X. Guo and J. Huang, *Chem. Commun.*, 2013, **49**, 704.

8942 | *J. Mater. Chem. C*, 2017, **5**, 8936–8943

This journal is © The Royal Society of Chemistry 2017

46 Y. Qiao, Y. Y. Lin, Y. J. Wang, Z. Y. Yang, J. Liu, J. Zhou, Y. Yan and J. B. Huang, *Nano Lett.*, 2009, **9**, 4500.

47 G. B. Deacon and R. J. Phillips, *Coord. Chem. Rev.*, 1980, **33**, 227.

48 K. Nakamoto, *Infrared and Raman Spectra of Inorganic and Coordination Compounds*, Wiley, New York, 5th edn, 1997.

49 M. Ornatska, S. Peleshanko, B. Rybak, J. Holzmueller and V. V. Tsukruk, *Adv. Mater.*, 2004, **16**, 2206.

50 B. Stevens and M. I. Ban, *Trans. Faraday Soc.*, 1964, **60**, 1515.

51 R. F. Fink, J. Seibt, V. Engel, M. Renz, M. Kaupp, S. Lochbrunner, H. M. Zhao, J. Pfister, F. Wurthner and B. Engels, *J. Am. Chem. Soc.*, 2008, **130**, 12858.

52 X. H. Cao, L. Y. Meng, Z. H. Li, Y. Y. Mao, H. C. Lan, L. M. Chen, Y. Fan and T. Yi, *Langmuir*, 2014, **30**, 11753.

53 V. V. Tsukruk and V. V. Shilov, *Structure of Polymeric Liquid Crystals*, Naukova Dumka, Kiev, USSR, 1990.

54 M. I. A. el Maaty and D. C. Bassett, *J. Macromol. Sci., Part B: Phys.*, 2003, **B42**, 687.

55 I. V. Zatovsky, N. Y. Strutynska, I. V. Ogorodnyk, V. N. Baumer, N. S. Slobodyanik, M. M. Yatskin and I. V. Odynets, *Struct. Chem.*, 2016, **27**, 323.

56 S. C. Abrahams, *Acta Crystallogr., Sect. B: Struct. Sci.*, 2006, **62**, 26.

57 M. Blaise and S. Thirup, *Acta Crystallogr., Sect. F: Struct. Biol. Commun.*, 2011, **67**, 114.

58 S. Chen, P. Slattum, C. Y. Wang and L. Zang, *Chem. Rev.*, 2015, **115**, 11967.

59 Y. Che, X. Yang, G. Liu, C. Yu, H. Ji, J. Zuo, J. Zhao and L. Zang, *J. Am. Chem. Soc.*, 2010, **132**, 5743.

60 L. Zang, Y. Che and J. S. Moore, *Acc. Chem. Res.*, 2008, **41**, 1596.

61 Q. Zhao, Y. Wang, Y. Qiao, X. Wang, X. Guo, Y. Yan and J. Huang, *Chem. Commun.*, 2014, **50**, 13537.

62 S. R. Forrest, M. L. Kaplan, P. H. Schmidt, T. Venkatesan and A. J. Lovinger, *Appl. Phys. Lett.*, 1982, **41**, 708.

63 Z. Chen, V. Stepanenko, V. Dehm, P. Prins, L. D. A. Siebbeles, J. Seibt, P. Marquetand, V. Engel and F. Wuerthner, *Chem. – Eur. J.*, 2007, **13**, 436.